

MEASURING THE STANDARD MODEL AND SEARCHING FOR
NEW PHYSICS WITH JET SUBSTRUCTURE USING THE ATLAS DETECTOR

A DISSERTATION
SUBMITTED TO THE DEPARTMENT OF PHYSICS
AND THE COMMITTEE ON GRADUATE STUDIES
OF STANFORD UNIVERSITY
IN PARTIAL FULFILLMENT OF THE REQUIREMENTS
FOR THE DEGREE OF
DOCTOR OF PHILOSOPHY

Maximilian Swiatlowski
March 2015

© Copyright by Maximilian Swiatlowski 2015
All Rights Reserved

I certify that I have read this dissertation and that, in my opinion, it is fully adequate in scope and quality as a dissertation for the degree of Doctor of Philosophy.

(Ariel Schwartzman) Principal Adviser

I certify that I have read this dissertation and that, in my opinion, it is fully adequate in scope and quality as a dissertation for the degree of Doctor of Philosophy.

(Su Dong)

I certify that I have read this dissertation and that, in my opinion, it is fully adequate in scope and quality as a dissertation for the degree of Doctor of Philosophy.

(Jay G. Wacker)

I certify that I have read this dissertation and that, in my opinion, it is fully adequate in scope and quality as a dissertation for the degree of Doctor of Philosophy.

(Blas Cabrera (??))

I certify that I have read this dissertation and that, in my opinion, it is fully adequate in scope and quality as a dissertation for the degree of Doctor of Philosophy.

(???)

Approved for the Stanford University Committee on Graduate Studies

Preface

This thesis tells you all you need to know about...

Acknowledgments

I would like to thank...

Contents

Preface	v
Acknowledgments	vi
1 Introduction	1
2 The Standard Model, and the Theory of Strong Interactions	2
2.1 Overview	2
2.2 Spontaneous Symmetry Breaking, the Electroweak Force, and the Origin of Mass	2
2.3 Quantum Chromodynamics and Strong Interactions	2
3 Jets and Substructure	3
3.1 The Goal of Jets, and Jet Algorithms	3
3.2 Jet Substructure: Going Deeper	3
3.3 Calculations with Jets	3
4 Supersymmetry, <i>R</i>-Parity, and Naturalness	4
4.1 The Problem of the Standard Model	4
4.2 Supersymmetry: The Solution?	4
4.3 <i>R</i> -Parity, and How to Violate It	4
4.4 Naturalness, or the Pursuit of Beauty	4
5 The Large Hadron Collider	5
5.1 History	5
5.2 Machine Design	10
5.3 Luminosity, and Pileup	10
5.4 Operations in 2010-2012	10
6 The ATLAS Detector	11
6.1 History	15

6.2	Magnet Systems	17
6.2.1	Solenoid	19
6.2.2	Barrel toroids	19
6.2.3	Endcap toroids	20
6.3	Inner Detector	20
6.3.1	Silicon Pixel Detector	22
6.3.2	Silicon Strip Tracker	24
6.3.3	Transition Radiation Tracker	25
6.4	Calorimeters	27
6.4.1	Electromagnetic Calorimeter	28
6.4.2	Hadronic Calorimeter	32
6.5	Muon Spectrometer	36
6.6	Triggering	36
6.7	Data Quality	36
7	Jet Reconstruction with ATLAS	37
7.1	Clusters, Towers, and Tracks, Oh My	37
7.1.1	Cluster Calibration	37
7.2	Jet Calibration	37
7.3	Quark/Gluon Discrimination	37
7.3.1	Lots of subsections	37
8	Seeing Color at the LHC	38
8.1	Motivation	38
8.2	Reconstructing Color	38
8.2.1	Finding Top Quarks	38
8.2.2	Origin Corrections	38
8.2.3	Resolution Effects	38
8.2.4	Track and Cluster Uncertainties	38
8.3	Measuring Color	38
8.3.1	Unfolding	38
8.3.2	Results	38
8.3.3	Future Prospects	38
9	Searching for Supersymmetry with Super Jets	39
9.1	Motivation	39
9.2	Why Jet Substructure?	39
9.2.1	Total Jet Mass, and Other Variables	39

9.2.2	Jet Mass Templates	39
9.3	Constructing a Search	39
9.3.1	Background Estimates	39
9.3.2	Limits	39
9.3.3	Future Prospects	39
10	Conclusions	40
A	A Long Proof	41
	Bibliography	42

List of Tables

List of Figures

5.1	An aerial view of Geneva, with the location of the LHC superimposed. The individual detectors (described in chapter 6, as well as the main CERN Meyrin site, are also highlighted. Image courtesy CERN.	6
5.2	A schematic drawing of the initial design of a shared LEP/LHC tunnel, with the LHC beamline positioned on top of the existing LEP beamline [1].	8
5.3	A photo of the final LHC tunnel, no LEP beamline, in contrast to the first plans shown in Figure 5.1. Photo courtesy of USLHC.	9
6.1	A schematic diagram of the interactions of various particles with detector components. Copyright CERN.	12
6.2	A computer-generated view of the ATLAS detector, with people for scale. Copyright CERN.	14
6.3	An early view of a potential superconducting air-core toroid magnet system for the ATLAS detector from the 1992 Letter of Intent [2].	16
6.4	A view of the ATLAS cavern during construction. Copyright CERN.	16
6.5	ATLAS recorded luminosity as a function of date in 2011 and 2012. The yellow show all data delivered by the LHC, green was recorded by ATLAS, and blue was high-quality data.	17
6.6	A computer generated visualization of the ATLAS magnet systems.	18
6.7	A photograph of the ATLAS solenoid shortly after the winding of the coils was finished. Copyright CERN.	19
6.8	A photograph of the ATLAS barrel toroids after their installation. Note person in the center for scale. Copyright CERN.	20
6.9	A photograph of an ATLAS endcap toroid shortly before its installation in the detector. Copyright CERN.	21
6.10	A computer-generated view of the ATLAS inner detector, with relevant sizes of the detector marked out. Copyright CERN.	22

6.11	A cut-out view of the ATLAS inner detector, showing the layers a particle would interact with as it passed outward from the collision point. Copyright CERN.	23
6.12	A cut-out view of the Inner Detector and the locations in r , z (with lines of detector η demarcated) of the various detector subsystems.	23
6.13	A computer-generated view of the ATLAS pixel detector. Copyright CERN.	25
6.14	A photograph of one segment of the ATLAS SCT endcap disks. Copyright CERN.	26
6.15	A photograph of the ATLAS TRT system during testing. Copyright CERN.	27
6.16	A computer generated image of the ATLAS calorimeter system, showing the locations of each different subdetector. Copyright CERN.	28
6.17	A photograph of the accordion structure used in the LAr barrel. Copyright CERN.	29
6.18	A drawing of a LAr module near $\eta = 0$. The relative size of each layer in the module, in both length and radiation lengths, is shown.	30
6.19	A photograph of the LAr endcap after installation in the cryostat system. Copyright CERN.	30
6.20	A plot of the LAr ionization pulse and the shaped output from the frontend electronics, including the negative energy region.	31
6.21	A plot the measured and predicted LAr energy distributions during a 2008 cosmic ray run.	32
6.22	A photograph of the installation of the barrel tile calorimeter. Copyright CERN.	33
6.23	A drawing of one wedge of the tile detector.	34
6.24	A photograph of one of the scintillating tiles which give the tile calorimeter its name. Copyright CERN.	35
6.25	A computer generated image showing the locations of each of the muon spectrometer subsystems. Copyright CERN.	35

Chapter 1

Introduction

...

Chapter 2

The Standard Model, and the Theory of Strong Interactions

2.1 Overview

2.2 Spontaneous Symmetry Breaking, the Electroweak Force, and the Origin of Mass

2.3 Quantum Chromodynamics and Strong Interactions

Chapter 3

Jets and Substructure

3.1 The Goal of Jets, and Jet Algorithms

3.2 Jet Substructure: Going Deeper

3.3 Calculations with Jets

Chapter 4

Supersymmetry, R -Parity, and Naturalness

4.1 The Problem of the Standard Model

4.2 Supersymmetry: The Solution?

4.3 R -Parity, and How to Violate It

4.4 Naturalness, or the Pursuit of Beauty

...

Chapter 5

The Large Hadron Collider

The Large Hadron Collider (LHC) is a 27 km long proton-proton (pp) synchotron built on the border of France and Switzerland, near the city of Geneva. The accelerator is nestled beneath mostly bucolic French farmland, as seen in Figure 5.

The total costs of the accelerator and the detectors it serves are estimated at \$20 billion, making the LHC one of the largest scientific enterprises ever attempted. [*Ed: cite this*] The project is full of similar superlatives: the accelerator is the largest machine, the ATLAS detector is the largest detector, the CMS detector is the heaviest. 10,000 scientists from 113 countries work on some aspect of the project, making it one of the best examples of international cooperation that mankind has produced.

The machine is composed of eight essentially identical sectors,

The machine was designed to deliver collisions at $\sqrt{s} = 14$ TeV energy at a rate of 10^{34} cm $^{-2}$ /s, but as of 2012 collisions had only occurred at 8 TeV and a rate of 5×10^{33} cm $^{-2}$ /s.

[*Ed: Describe sectors, luminosity, energy, helium*]

5.1 History

The LHC was first discussed publically at the ECFA-CERN Workshop held at Lausanne and Geneva in March of 1984 [1]¹. This was a very active time for proposing new collider experiments, as extensive work on the 40 TeV pp Superconducting Supercollider (to be built in Waxahachie, Texas) had recently displaced a proposal for a 4 TeV $p\bar{p}$ Dedicated Collider at Fermilab [1, 3], though construction continued on Fermilab's 2 TeV $p\bar{p}$ Tevatron collider. The Soviet Union was even planning a 6 TeV $p\bar{b}$ collider, the Accelerator and Storage Complex (UNK) [4][*Ed: This needs a better citation*]. In this busy landscape, the proposal of another machine at CERN– which was currently building the Large Electron Positron (LEP), the world's largest e^+/e^- collider– was very ambitious indeed.

¹4 years and 1 month before the author was born!



Figure 5.1: An aerial view of Geneva, with the location of the LHC superimposed. The individual detectors (described in chapter 6, as well as the main CERN Meyrin site, are also highlighted. Image courtesy CERN.

Several characteristics made the proposed LHC unique and worth pursuing in such a competitive environment. First, with the construction of the LEP tunnel on track for completion in 1988, the civil-engineering component of the project was greatly reduced, especially compared to the enormous expense of constructing the SSC tunnel. Second, while the design goals of 20 TeV collisions were at a significantly lower energy than the SSC, the projected luminosity was eventually designed to be a factor of 10 higher ($10^{34} \text{ cm}^{-2}/\text{s}$, though the initial designs focused on $10^{33} \text{ cm}^{-2}/\text{s}$) and so the LHC could potentially gain sensitivity by accumulating data more quickly. Finally, as figure 5.1 shows, the initial designs for the LHC envisaged the LHC beamlines actually sitting on top of the existing LEP beamlines. The resulting hybrid collider would be able to run pp , ep , and ee collisions. This would not only extend the reach of the physics program by allowing for the study of deep inelastic scattering at higher energies than the HERA collider at DESY [*Ed: Cite this– HERA and e/p if possible.*], but would also allow for the study of Z bosons from ee , which could potentially be used as a calibration source for detectors before pp collisions [1].

With the approval of the SSC in 1987 and the subsequent start of construction in 1991, CERN was mostly focused on the construction and operation of LEP but did not stop planning for the LHC. This proved remarkably prescient, as in the face of changing budget priorities and the end of the Cold War, the SSC ended up being cancelled in 1993. [*Ed: This probably needs citations.*] CERN, on the other hand, approved a staged construction plan for the LHC in 1994, targetting first 10 TeV collisions in 2004 and then 14 TeV in 2008. Japan and the US joined CERN as observer states in 1995 and 1997 respectively, each contributing significantly to the construction of the LHC and joining the physics program of CERN.*[Ed: Statement about internation collaboration, compared to SSC? Statement about the 10 TeV plan being dropped?]*

The Conceptual Design Report [5] published in 1995 reflected the changed landscape with the demise of the SSC and the results of more detailed cost estimates. The design energy was lowered to 14 TeV– higher energies would have required more costly magnets– while the design luminosity was actually increased to $10^{34} \text{ cm}^{-2}/\text{s}$. This increase in luminosity came at a cost: the number of interaction points was reduced to four instead of eight, and only two would receive collisions at a high rate. [*Ed: Mention pileup here or no?*] Critically, it was also decided to remove the LEP beamline and magnets, as it was deemed too costly to follow the existing LEP infrastructure. While this reduced the physics program of the LHC substantially, being the only high energy hadron collider was still a rather broad portfolio.

With the shutdown of LEP in 2001², the construction of the LHC began in earnest. It would take till 2007 to install the last magnet in the LHC, and the detectors finalized their own installations only in 2008. Figure 5.1 shows the final state of the LHC tunnel (without the originally planned LEP beamline). The first low-energy collisions occurred on September 10, 2008, putting the LHC almost on track of its initial goal of 14 TeV collisions in 2008. [*Ed: Probably want to add a bit more*

²Not without controversy, as there was perhaps a tantalizing sign of an excess in Higgs-boson like events during the final runs of LEP.*[Ed: cite me]*

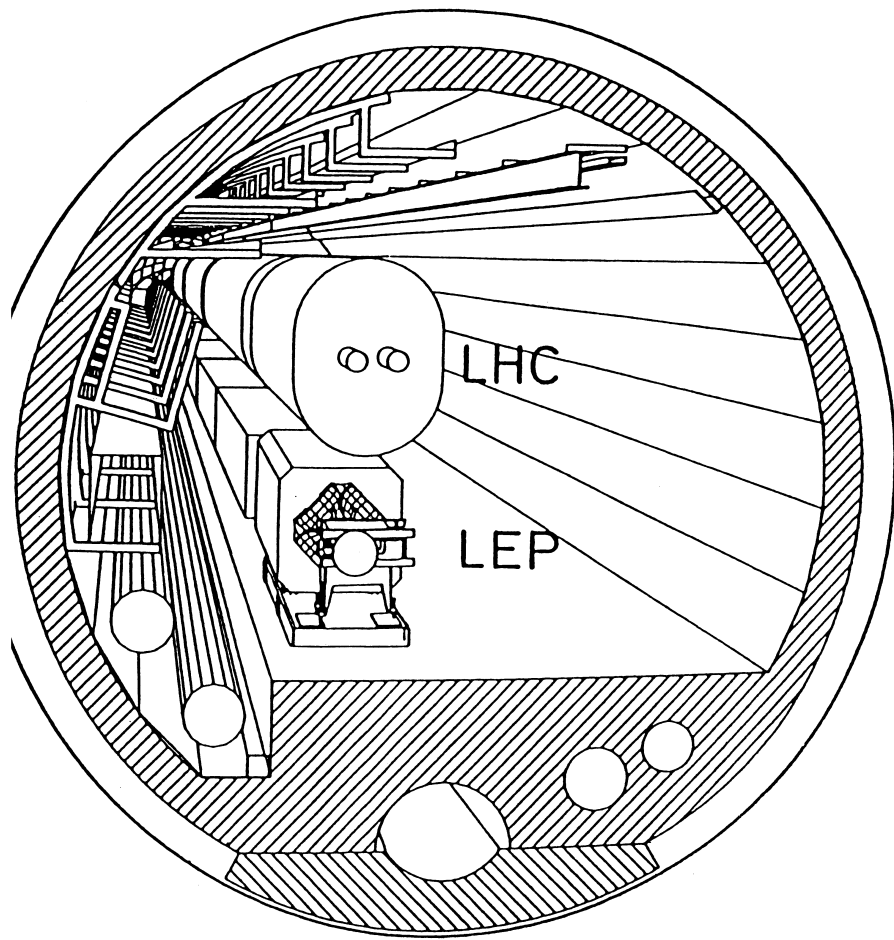


Figure 5.2: A schematic drawing of the initial design of a shared LEP/LHC tunnel, with the LHC beamline positioned on top of the existing LEP beamline [1].



Figure 5.3: A photo of the final LHC tunnel, no LEP beamline, in contrast to the first plans shown in Figure 5.1. Photo courtesy of USLHC.

on construction.]

However, an “incident” on September 19 ended up delaying the full startup for a year [6]. On that day, the operators were testing the last sector of the LHC at current levels appropriate for 5.5 TeV beams. A resistive zone developed in the electrical bus connection between a dipole and quadrupole magnet. While the power supply detected this and shut down within 0.39 seconds and the quench protection circuitry began to engage at 0.89 seconds, it was already too late: an electrical arc had sparked and punctured the liquid helium enclosure and the insulation vacuum along the cryostat. This, along with the electrical noise induced by the power supply shutdown and the heat dissipation caused by the quench protection circuitry, triggered a chain reaction in which several other magnets also began to quench and other vacuum systems were degraded. As the helium began to escape the cryostat, pressure relief valves correctly opened and vented the helium to atmosphere. However, an additional complication proved to be a problem: neighboring subsectors had their vacuum systems separated by vacuum barriers, meant to isolate the vacuum systems of neighboring areas. The vacuum barriers could only sustain a rather low pressure difference, and the extreme pressures generated by the evacuating helium overwhelmed these connections. The attendant large

pressure forces ended up displacing dipoles from their support structures, and knocked the cryostats from their support jacks— in some cases even ripping the anchors from the concrete floor. A total of six tons of helium, five quadrupoles, and twenty-four dipoles were lost in the incident.

Collisions would begin in earnest at a lowered energy of 7 TeV in 2010 and 2011. After two years of successful and safe operations at the reduced energy, 2012 saw a large increase in luminosity and an increase of the collision energy to 8 TeV. [*Ed: A bit more on operations at 8 TeV*.] The LHC then proceeded to shut down in 2013 until mid-2015 for a further round of repairs and consolidations of electrical connections to guarantee the safety of operations at near the design energy. As the restart of the LHC approaches in the coming months, we are anticipating collisions at 13 TeV with luminosity likewise reaching near design levels. The LHC will have broken energy records twice in the span of five years, making this an incredibly exciting time to be working in particle physics.

5.2 Machine Design

5.3 Luminosity, and Pileup

5.4 Operations in 2010-2012

Chapter 6

The ATLAS Detector

The design of the LHC, with two high-luminosity interaction points at opposite ends of the ring, called for two general purpose detectors to be built in these locations. Their charge was to accurately reconstruct collision events in the most hostile conditions yet seen in a collider: with a bunch spacing of 25 ns and the unprecedented introduction of pile-up the detectors would have an enormous challenge ahead of them in dealing with both the rate and the reconstruction of events. ATLAS (A Toroidal LHC APparatus) [7] and CMS (Compact Muon Solenoid) [8] were the two detectors built for this task, with ATLAS occupying the (much more convenient) Point 1 and CMS located at the (very distant) Point 5. The data presented in this thesis was collected by the ATLAS experiment in pp collisions at $\sqrt{s} = 8$ TeV in 2012.

Particle detectors measure particles via their interactions with matter, as drawn schematically in Figure 6. For example, charged particles (such as electrons and some hadrons) interact electromagnetically with silicon and gas tubes, leaving hits in different layers of detectors which can be traced back to form a track. Electrons and photons, with their low masses and high rate of interaction with matter, are measured by the electromagnetic calorimeter. The calorimeter is composed of alternating layers of metal meant to cause the particle to interact and lose energy, and active materials which measure the energy left behind in these interactions. The hadron calorimeter follows a similar principle, and alternately placed layers of metal and active material again aim to stop and measure the hadrons which the electromagnetic calorimeter did not stop. Muons, which do not interact very much with matter most matter but do leave hits in trackers, survive past even the hadronic calorimeter, and a special set of muon detectors can be used to identify them there. Neutrinos, as they interact with matter only via the weak force and thus very rarely, escape detection and are reconstructed only by inferring their presence from the lack of momentum conservation in the transverse plane.

A significant constraint in the design of detectors is the interaction of particles with matter. [**Ed:** *This needs citations.*] As particles traverse matter— including the detectors built to measure them—

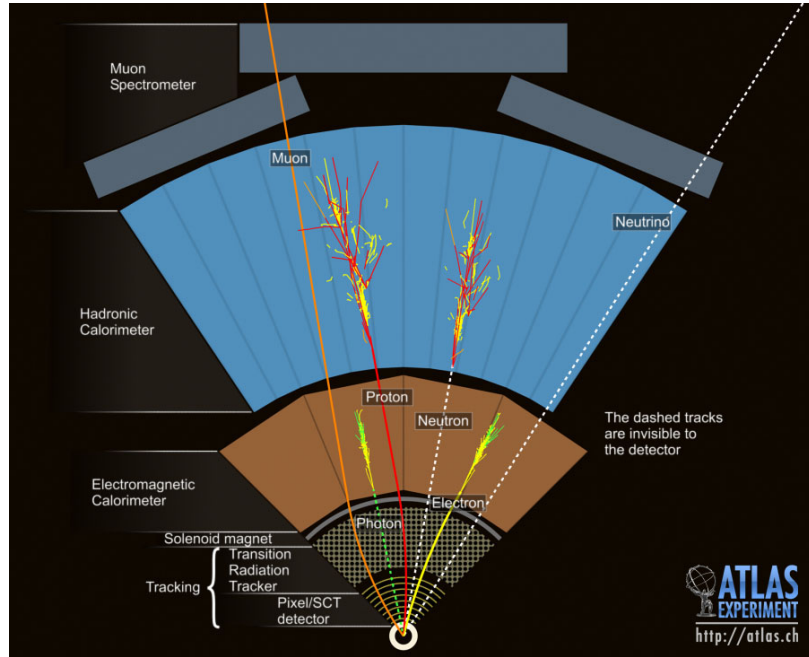


Figure 6.1: A schematic diagram of the interactions of various particles with detector components.
Copyright CERN.

they lose energy via interactions, or in the case of photons, can even convert into electron/positron pairs. As some detectors—particularly the calorimeters—sit radially behind others, this can mean that substantial portions of the energy of particles can have already dispersed by the time they are measured. One of the keys to an accurate detector, then, is to minimize the material before the calorimeters. [Ed: *Clean this up with better discussion of radiation lengths. Pages 350 of Perkins may be helpful*]

General purpose particle detectors thus demand the following characteristics: [Ed: *define radiation lengths? above?*]

1. Tracking systems must be able to identify primary and secondary vertices, while minimizing the radiation lengths before the calorimeters
2. Strong calorimetry systems are required to accurately measure the energy and position electrons, photons, and hadrons
3. Muon systems must be able to precisely reconstruct muons
4. All detector systems must be capable of being read out quickly, and a triggering system is required to quickly identify interesting events for recording

To this end, the ATLAS detector is built in the traditional onion-layer configuration, which measures particles as they travel perpendicular to the beam [7]. The Inner Detector, composed of the concentric Pixel, SCT [*Ed: define*], and Transition-Radiation-Tracker (TRT) subsystems, lies at the center of the detector and precisely measures tracks created by charged particles. A 2 T solenoid encloses the Inner Detector, bending charged particles and enabling the measurement of their momenta. Next the Electromagnetic Calorimeter (ECal), composed of liquid argon (LAr) and copper, sits outside of the solenoid in a liquid nitrogen cryostat, and measures energy deposits from electrons and photons (as well as hadrons to a lesser extent). The Hadronic Calorimeter, built to measure and stop any remaining hadronic particles, is composed of steel and scintillating tile in the center (referred to as the barrel), and LAr and copper in forward regions (referred to as end-caps). Surrounding these are an additional set of magnets: the superconducting air-core toroids of the barrel and endcaps, which bend particles in the plane perpendicular to that of the bending due to the solenoid. [*Ed: That needs cleaning.*] The Muon Spectrometer (composed of MDT, RPC, TGC, and CSC subsystems) sits outside of (and next to) these magnets, and provides a final measurement of the charged particles which reach that far. The entire detector is shown in Figure 6. The incredible size of the detector—25 m in diameter, and 46 m long—is dominated by the Muon Spectrometer and the toroids. On the other hand, the detector is comparatively light (only 7000 tons, compared to 14,000 tons for CMS), as the air-core toroids do not add substantial weight to the detector [8, 7].

In keeping with the principle of “similar, but opposite” established by their locations, the ATLAS and CMS detectors take complementary approaches to the various aspects of event reconstruction in collisions. All general purpose detectors have the same basic goals: they must reconstruct the outgoing, stable particles produced in collisions and the subsequent decays of particles in these collisions. Different particles are detected with different general classes of detectors, of which there are many possible types. For example, electrons and photons are measured by the ECal, for which ATLAS used a liquid argon (LAr) and copper system while CMS used a crystal lead tungstate system. Each had their own advantages and disadvantages (ATLAS’s was less costly and already proven technology with better position resolution, while CMS took a riskier route which promised better energy resolution), but overall performance between the detectors tends to be very similar because of various trade-offs. In the case of the ECals, the precision of ATLAS and CMS’s $H \rightarrow \gamma\gamma$ measurements ended up being largely similar [*Ed: cite?*], in no small part because CMS’s all-silicon tracking system introduced greater radiation lengths before the calorimeters, thereby prompting more photons to convert and losing precision in the measurement. On the other hand, CMS’s comparatively weak brass hadronic calorimeter (compared to ATLAS’s higher resolution tile calorimeter), is compensated by their tracking system, which enables a particle-flow reconstruction algorithm to combine information from all detectors and improve jet performance to levels very similar to ATLAS. [*Ed: consider citations, and substantial revisions here*]. Similarly, the large size and extra toroid magnets of ATLAS allow for a larger lever-arm and an additional set of

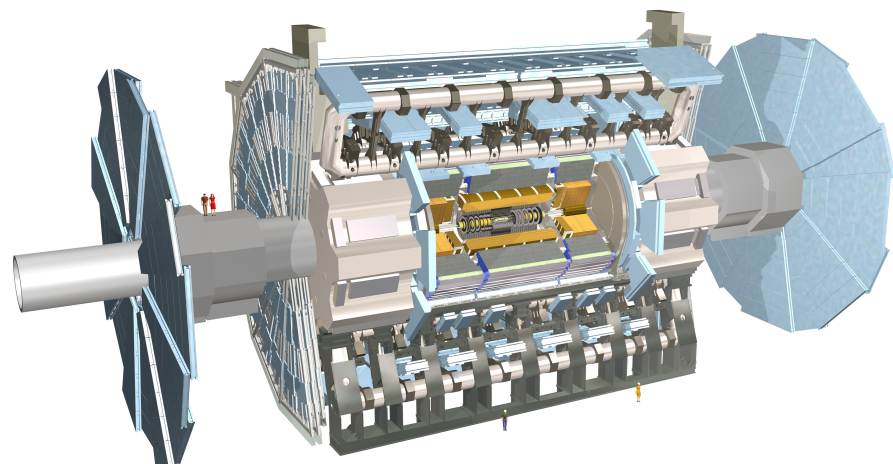


Figure 6.2: A computer-generated view of the ATLAS detector, with people for scale. Copyright CERN.

measurements of muons (enabling reconstruction with or without the inner detector): however, muon reconstruction performance in CMS is very similar because the stronger solenoidal magnetic field (4 T compared to 2 T) allows for a better measurement using the inner detector only (with the muon systems on CMS providing only a tag of a passing muon, and not a complete reconstruction).

6.1 History

The first public discussion of the proposals which became the ATLAS detector occurred in 1992 at the General Meeting on LHC Physics at Evian-les-Bains [9, 10]. At the time, four general purpose detectors (much like the four detector configuration in place at LEP) were seriously considered: EAGLE, ASCOT, CMS, and L3 (as an upgrade to the existing LEP detector, including a movable stage which would allow it to take data from both e^+ / e^- and pp collisions). Several additional single purpose (heavy ion, neutrino, and B -physics) detectors were also proposed.

ATLAS emerged in a later 1992 Letter of Intent as a merger of the ASCOT and EAGLE collaborations [2]. ASCOT (Apparatus with SuperCOnducting Toroids) contributed the physically-defining feature of the secondary toroidal magnet system and standalone muon measurement system, as well as the tradition of using a tortured amalgamation of letters to form a name. EAGLE (Experiment for Accurate Gamma, Lepton and Energy measurements) on the other hand featured a stronger 2 T magnetic field, and inner-detector and calorimeter designs more similar to some of the final ATLAS systems. The detector described in the Letter of Intent already resembled ATLAS in many important ways, featuring the superconducting air-core toroids, accordion-shaped liquid Argon electromagnetic calorimeters, scintillating tile hadron calorimeters, and multi-design inner detector. 6.1 shows an early drawing of ATLAS from the Letter, and already the detector looks recognizable to its current form.

By the release of the 1994 Technical Proposal [11], the detector design was becoming much more complete, and many of the choices of design for the detector subsystems (the components of the ID, for example) were already mostly complete. By 1997 many of the detector subsystem Technical Design Reports (TDR) were complete, and construction began on these systems [12]. 1999 saw a TDR for the entire detector, representing a complete integrated design for the entire detector [13, 14]. Memoranda of Understanding with national funding institutions are completely arranged by 2000, as construction of the detector is well underway [12]. The cavern, the largest yet built at CERN and pictured in Figure 6.1, is completed in 2003. Assembly of detector components continues rapidly at this point, and the detector is finished in 2008.

Early data-taking was of course disrupted by the incident described in Section 5.1, and first 7 TeV collisions were recorded on March 3, 2010. ATLAS recorded 35 pb^{-1} in 2010, 4.6 fb^{-1} in 2011, and 20.3 fb^{-1} in 2012. Figure 6.1 shows the dramatic increase of data during 2011 and 2012, which came at the cost of pileup levels higher than what had been planned for. The detector had an

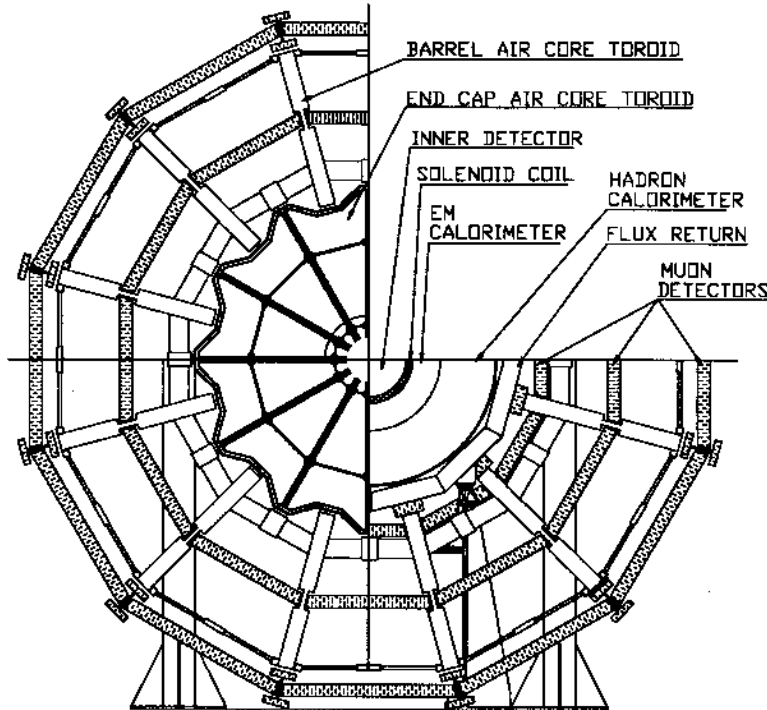


Figure 6.3: An early view of a potential superconducting air-core toroid magnet system for the ATLAS detector from the 1992 Letter of Intent [2].



Figure 6.4: A view of the ATLAS cavern during construction. Copyright CERN.

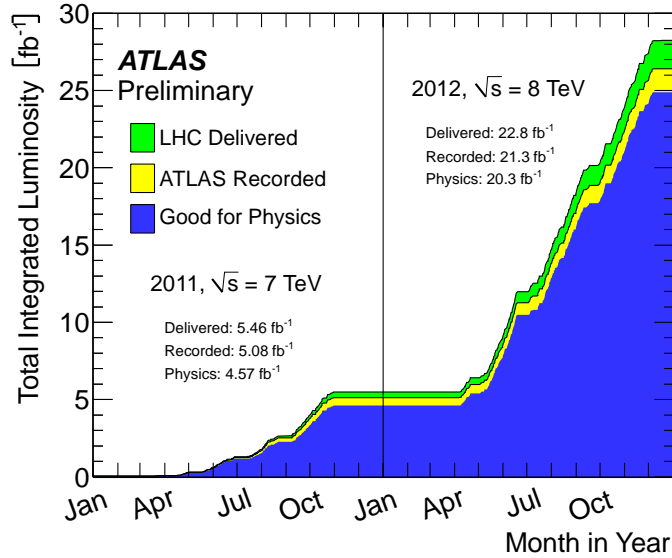


Figure 6.5: ATLAS recorded luminosity as a function of date in 2011 and 2012. The yellow show all data delivered by the LHC, green was recorded by ATLAS, and blue was high-quality data.

impressive uptime during collisions, with more than 90% of delivered collisions usable for physics.

6.2 Magnet Systems

The magnets of ATLAS play a critical role in the measurement of particle momenta by bending charged particles via the interaction with the Lorentz Force Law:

$$\frac{d\vec{p}}{dt} = q(\vec{E} + \vec{v} \times \vec{B}) \quad (6.1)$$

where \vec{p} is the particle 4-momentum, q is the charge, v is the velocity, and E and B are the electric and magnetic fields. The solenoid, for example, has a field in z direction only, resulting in a force in the ϕ direction. As the magnetic field does no work, the energy of the particle is not changed, and only the direction is affected. The degree of bending is directly proportional to \vec{v} , the velocity, and so the particle's momentum is able to be extracted. The field configuration in the toroid systems is much more complicated, but the particle momentum reconstruction follows the same general principle. [*Ed: Clean this up, and cite.*]

The combined magnet system is shown in Figure 6.2. The solenoid sits at the center, and the toroid system on the outside and in the endcaps.

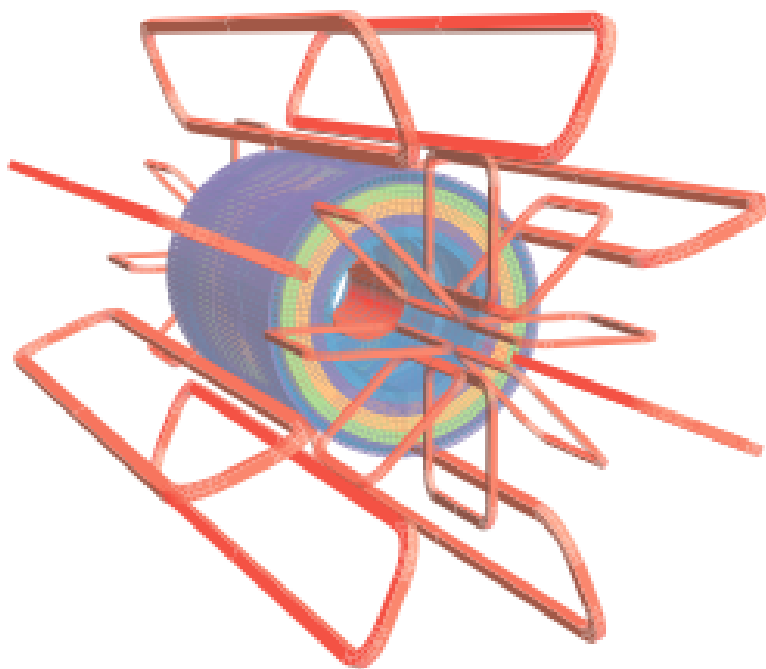


Figure 6.6: A computer generated visualization of the ATLAS magnet systems.



Figure 6.7: A photograph of the ATLAS solenoid shortly after the winding of the coils was finished.
Copyright CERN.

6.2.1 Solenoid

ATLAS's solenoid is shown in Figure 6.2.1 shortly after its construction was finished. It sits inside the calorimeter systems, and surrounds the Inner Detector. This is contrast to the configuration in CMS, where their solenoid surrounds the calorimeter systems. Thus, particles in ATLAS do not bend in the calorimeters and particle showers tend to be more directly collimated, while particles tend to be dispersed much further in the calorimeter in CMS.

The ATLAS solenoid has a 2 T axial field, powered by 7.730 kA of current [7]. Since the solenoid is in front of the calorimeters, care must be taken to reduce the material that particles can interact with. To that end, the magnet and the LAr calorimeter share the same vacuum vessel, eliminating the need for two additional walls. The magnet is composed of Al-stabilized NbTi conductor, developed specifically to best balance high field and low thickness. The solenoid occupies the space between 2.46 and 2.56 m, and is 5.8 m long axially. The stored energy of the magnet system is approximately 40 MJ, and it takes approximately a week to cool the magnet to the operational temperature of 4.5 K.

6.2.2 Barrel toroids

The ATLAS magnet system contains two separate toroids systems [7]. The barrel toroid consists of 8 coils in separate racetrack-configured, stainless-steel vacuum vessels which give the ATLAS the detector its famous shape, as seen in Figure 6.2.2. The magnets are supported by a system of 8

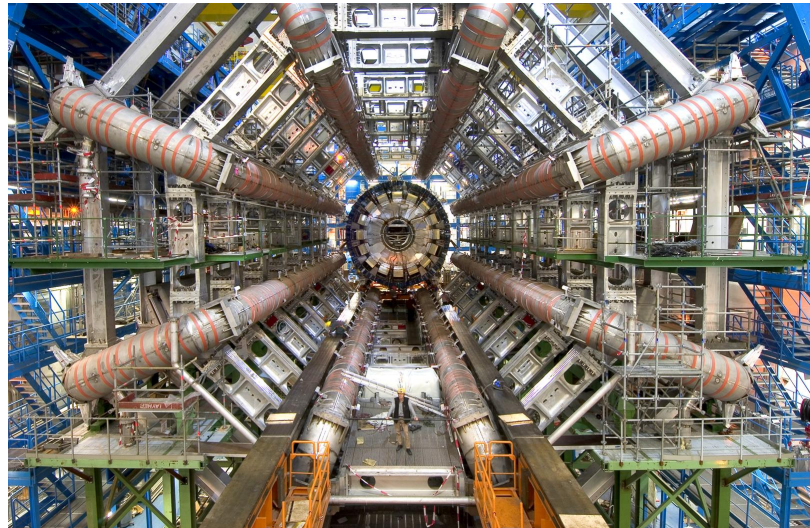


Figure 6.8: A photograph of the ATLAS barrel toroids after their installation. Note person in the center for scale. Copyright CERN.

inner and 8 outer support rings. The entire system is 25.3 m long, and begins at 9.4 m radially and ends at 20.1 m. The magnet is composed of the same wire as used in the solenoid, and the magnet system stores 1.1 GJ of energy during operation at 20.5 kA of current. The barrel toroid takes approximately 5 weeks to cool to its nominal temperature of 4.6 K.

6.2.3 Endcap toroids

The third ATLAS magnet system are the endcap toroids [7]. These magnets are designed bend the muons which interact with the muon spectrometer endcaps. They are constructed to be removable in order to allow access to the calorimeter and inner detector systems. The endcaps are each constructed of 8 flat, square coils with 8 keystone wedges which share the same cryostat. The magnets each take four weeks to cool to the operating temperature of 4.5 K, and operate at 20.5 kA with a stored energy of 0.25 MJ each. The coil material is again largely similar to that of the barrel toroid and solenoid. One of the endcap toroids is pictured in Figure 6.2.3 after being lowered into the ATLAS cavern.

6.3 Inner Detector

The ATLAS Inner Detector (ID) sits at the center of the experiment [7]. The purpose of the detector is to reconstruct the tracks (i.e. trajectories) of charged particles produced by the collisions of the LHC in order to not only accurately measure the locations of primary and secondary vertices, but to also directly measure the momenta and locations of charged particles [15]. The detector covers



Figure 6.9: A photograph of an ATLAS endcap toroid shortly before its installation in the detector. Copyright CERN.

the range $|\eta| < 2.5$, and is capable of measuring particle momenta as low as $p_T = 500$ MeV. Charged particle reconstruction efficiencies are typically greater than 90% for 100 GeV particles and 70% for 1 GeV particles, with a strong η dependence. Typical p_T resolutions are of order $0.05\%\text{GeV}^{-1} \times p_T \oplus 1\%$, and impact parameter resolutions are approximately $10 \mu\text{m}$ ¹.

The ID is composed of several independent detector subsystem which read out the locations of interactions with charged particles. These hits are fit to tracks by a suite of tools, which include standard global- χ^2 and Kalman-filters, but also several specialized fitters [15]. The p_T of the particles is obtained by measuring the curvature produced by the 2 T solenoid (as described by Section 6.2.1) surrounding the detector. The three subsystems, described below, are the silicon pixel tracker (Pixel), silicon microstrip tracker (SCT), and transition radiation tracker (TRT). The combined detector has a length of 7024 m and a radius of 1.15 m [7]. Figure 6.3 shows a computer generated image of the combined ID, and Figure 6.3 shows a computer-generated image of the various subcomponents of the ID and their spacing. Figure 6.3 shows the η range of the various detector subsystems, displaying the transition between barrel and endcap components.

At design luminosity, the detector is expected to measure approximately 1000 charged particles every 25 ns within the detector acceptance [15]. The added growth of pileup in the 2012 and future LHC runs have increased the importance of the Inner Detector as the primary vertex identification has become even more critical [16], but growing challenges from the computing time necessary to fit so many tracks (which increase more than quadratically as the number of detector hits [17]) will

¹The impact parameter is the perpendicular distance from the origin to the point of closest approach of the track, and is critical for the measurement of secondary vertices.

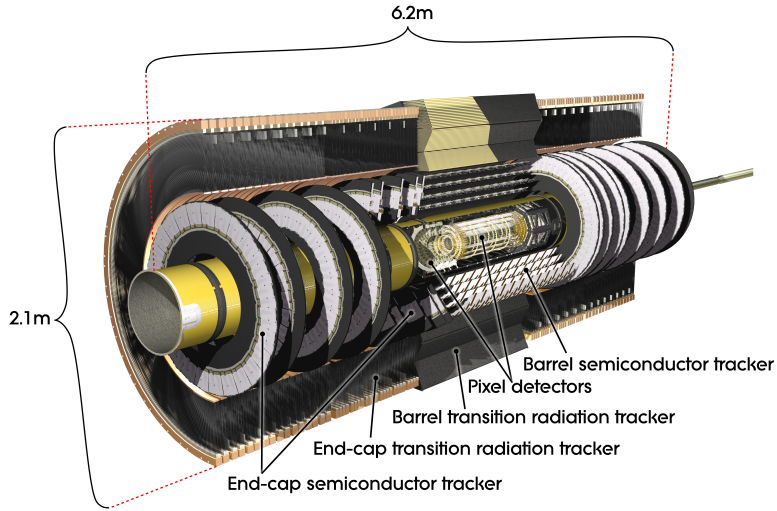


Figure 6.10: A computer-generated view of the ATLAS inner detector, with relevant sizes of the detector marked out. Copyright CERN.

also need to be overcome to make best use of the detector's information.

6.3.1 Silicon Pixel Detector

The innermost ATLAS sub-detector is the Silicon Pixel Detector [18, 7]. The principal of detection for the pixel detector follows the standard ionizing radiation detector [19]. Charged particles interact with the active medium (doped silicon), knocking electrons loose from their host atoms and creating electron-hole pairs. An applied voltage carries the holes and electrons to opposite ends of the detectors, where they are read out. The active regions are very small in both x and y dimensions, allowing for many independent measurement channels in a small area. Given the high number of particles expected from LHC collisions, and that the density is greatest nearest to the interaction point, it is critical that the innermost detector have a huge number of very small channels, making the task perfectly suited for a pixel detector.

80.4 million independent pixel channels, with a size of $50 \times 400 \mu\text{m}$, are read out by 1744 bump-bonded modules attached to the active sensors. Each of the modules are composed of 16 radiation hard front-end chips [7]. This corresponds to a combined active area of 1.7 m^2 . The detector is arranged in three radial layers in the barrel section, and three disks in the end-caps. In the radial layers, the pixels have a resolution of $10 \times 115 \mu\text{m}$ in $R - \phi$ and z respectively, and in the end-caps the orientation is perpendicular and the resolution is $10 \times 115 \mu\text{m}$ in R and $R - \phi$: the orientations are always chosen such that the most precise measurement takes place in the direction most relevant

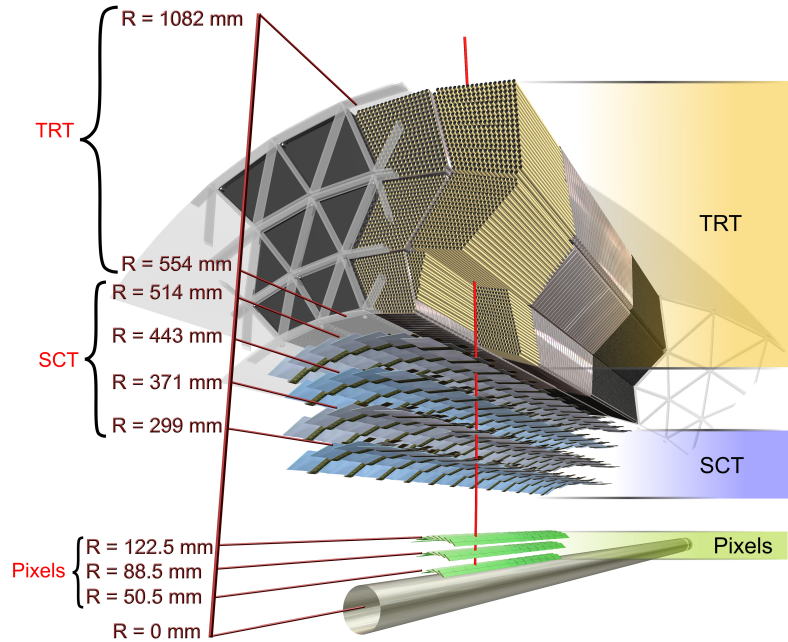


Figure 6.11: A cut-out view of the ATLAS inner detector, showing the layers a particle would interact with as it passed outward from the collision point. Copyright CERN.

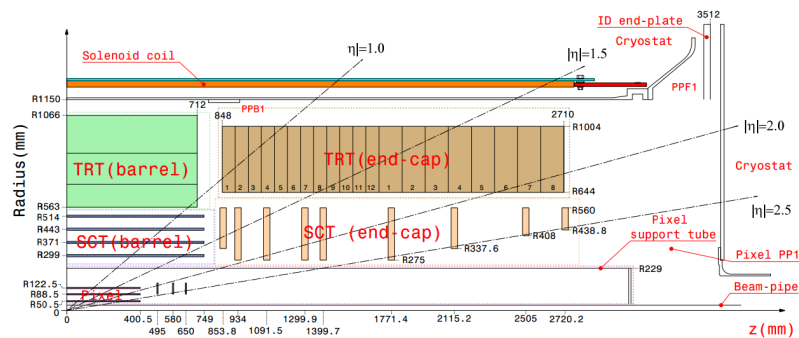


Figure 6.12: A cut-out view of the Inner Detector and the locations in r , z (with lines of detector η demarcated) of the various detector subsystems.

to the measurement of the track p_T .² The barrel and disk arrangement is shown in Figure 6.3.1. Hits are read out when charge has been collected over a tunable threshold determined by the noise of each pixel, resulting in typical occupancies of $10^{-4} - 10^{-5}$, though this grows obviously grows with additional pp interactions.

The innermost radial layer, known as the *b*-layer, sits only 50.5 mm from the center of the beampipe, while the outermost layer is located at 122.5 mm [7]. By placing detectors so close to the interaction point, it is possible to very accurately measure the location of both primary vertices—the locations of pp collisions—and second vertices—the locations of the displaced decays of particles with long lifetimes, such as *B*-hadrons [15].

Placing the detector so close to the beamline comes at a price, however, as the detector is particularly susceptible to radiation damage due to the high flux of particles through a small area. At design luminosity, this is expected to be about 158 kGy/year at the *b*-layer, reduced to 25.4 kGy/year at the outermost layer [7]. Damage comes in the form of displaced atoms in the doped silicon lattice, resulting in lower electron-hole yields per particle interaction. Some of the damage is mitigated by operating at cold temperatures (typically -5 to -10° C), and higher bias voltages can also alleviate the effects.

While the entire Inner Detector is expected to be replaced after 300 fb^{-1} are collected in order to replace the damaged components, the long shutdown of 2013-2015 presented ATLAS with the opportunity to augment the existing pixel detector with the so-called Insertable B-Layer (or IBL) [20]. The IBL, which adds an additional layer of pixels to the barrel and endcap pixel systems, is attached directly to a new carbon-fiber beampipe, and is located only 33 mm from the center of the beampipe. Due to this extremely close distance, the pixel size has been further reduced to $50 \times 250 \mu\text{m}$. The vertexing performance (especially secondary vertex identification for *b*-tagging) of ATLAS in Run 2, starting in 2015, is expected to substantially increase due to the IBL.

6.3.2 Silicon Strip Tracker

The next outermost subdetector in the ID is composed of silicon microstrip layers [21, 7], and is commonly referred to as the SCT. The SCT operates under a very similar principal to the Pixel detector: doped silicon under an electric bias is the active medium, and electron/hole pairs are collected to read out hits. Unlike the Pixels, one dimension of the detector is ganged together to form the eponymous strips. Two sets of detectors must therefore placed perpendicularly to each other (or at some other angle) to provide a true two-dimensional measurement, but the number of channels to be read out has been significantly reduced [19].

The ATLAS SCT contains 4088 modules, each composed of two 64 mm silicon strip sensors with a 40-mrad angular offset [7]. Like the Pixels, the detector is arranged into radial layers in the barrel and disks in the endcap, of which there are 4 and 9 respectively. The strips have a resolution of

²The $R - \phi$ coordinate is simply a distance-projected version of the azimuthal angle ϕ .

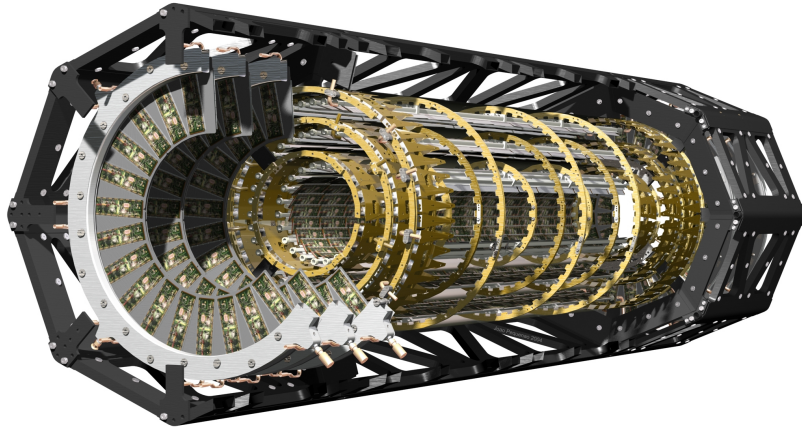


Figure 6.13: A computer-generated view of the ATLAS pixel detector. Copyright CERN.

17×580 in $R - \phi$ and z respectively in the barrel, and 17×580 in $R - \phi$ and R in the disks. The SCT occupies the space between 275 mm and 560 mm from the beamline. The detector contains a total of 6.3 million read out channels read out by radiation hard front-end chips [22]. The increased distance of the SCT from the beamline significantly lowers the rate of expected radiation damage, but increased bias voltages are still expected to be necessary after significant luminosity [21, 7]. Figure 6.3.2 shows one segment of the SCT endcap disks.

6.3.3 Transition Radiation Tracker

The final subdetector of the ID is the transition radiation tracker [7]. Unlike the other subdetectors of the ID, the TRT is not made out of silicon: instead, it is composed of 2 mm (in radius) straw tubes (proportional drift tubes) [7]. The tubes detect particles via ionization: particles traversing the tube interact with the gas in the tube (70 % Xe, 27 % CO₂, and 3 % O₂) and create ion/electron pairs [19, 7]. The exterior of the tube is a cathode, and a center wire is an anode, set at a voltage difference of 1530 V. The extreme electric field in the tube accelerates the electrons rapidly through the gas, colliding with other atoms and creating more ion/electron pairs, creating an avalanche which greatly amplifies the original signal [19]. The time of arrival of the signal to the anode depends on the position of the initial collision and the known drift velocity of the gas, thus allowing for an accurate radial measurement of the interaction point [23], but no information about the location of the interaction along the length of the tube.

The TRT covers the range $|\eta| < 2.0$ in the standard barrel and endcap arrangements [24]. There are 52544 tubes, each 1.44 m in length, arranged in two active regions on either side of the center of the detector. The endcaps are each composed of 122880 370 mm long tubes, organized into 18 wheels. The barrel is arranged in layers of 76 straws, while the endcaps have 160 planes. There are

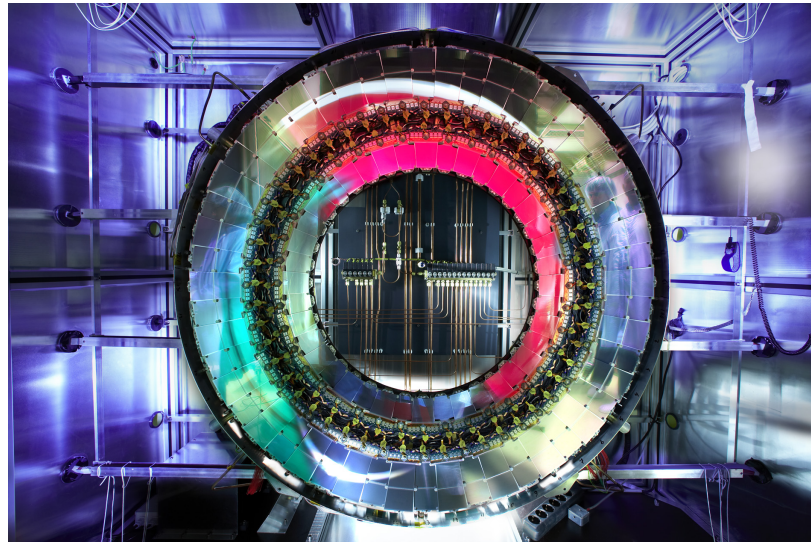


Figure 6.14: A photograph of one segment of the ATLAS SCT endcap disks. Copyright CERN.

a combined 350848 channels in the detector. Figure 6.3.3 shows a photograph of the TRT barrel during testing.

The TRT, whose active elements are much larger than that of the silicon sensors in the rest of the ID, has a significantly larger hit resolution: $130 \mu\text{m}$ in $R - \phi$ [7]. This is partly compensated by the large number of straws that charged particles cross, generating on average 30 hits [15]. The TRT has the added benefit of providing identification of electrons via the emission of transition X-rays [25]. X-ray photons can be emitted as a relativistic electron passes through materials with different dielectric constants; the X-rays can subsequently interact with the straw tube gas and cause an ionization with a much higher energy than for a direct hit (15 keV, compared to 2 keV) [23]. This extra energy can be recorded and used later for identification of the electron. In the barrel, the TRT straws are embedded in a set of polypropylene-polyethylene fibers with a diameter of $19 \mu\text{m}$; in the endcap, foil is interleaved between the straws. This type of identification is not possible with silicon detectors, providing the TRT with a unique capability. Finally, the gas tubes of the TRT present a significantly lower amount of material to particles traversing the ID compared to silicon detectors, thereby degrading less the performance of the ECal and HCal.

Given the distance of the TRT from the interaction point, and the greater resilience of gas tubes to radiation compared to silicon (there is no atomic lattice to be damaged), the TRT is not expected to be significantly damaged during the course of data-taking. However, with the presence of increasing pileup conditions in upcoming runs, the occupancy of the TRT is expected to grow significantly, presenting a significant challenge to continued operation [26].

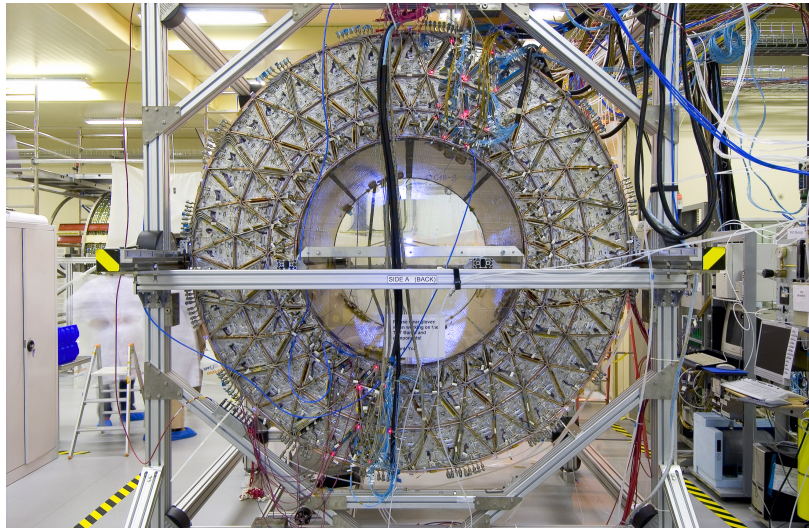


Figure 6.15: A photograph of the ATLAS TRT system during testing. Copyright CERN.

6.4 Calorimeters

The ATLAS calorimeters lie outside of the ID and the solenoid, and are responsible for a near-hermetic ($|\eta| < 4.9$) measurement of all particles except for muons and neutrinos [7]. The calorimeter system is also critical in stopping particles (besides muons) from entering the muon spectrometer. The calorimeters are the primary detectors of interest in the reconstruction of hadronic events, as they are the only detectors capable of measuring neutral particles which the tracker can miss. The operation of these detectors is thus critical for both searches for new physics in hadronic channels, and for measurements of hadronic phenomena in the Standard Model.

The combined calorimeter system is pictured in Figure 6.4. There are several subsystems: the LAr electromagnetic barrel, the tile barrel, tile extended barrel, the LAr electromagnetic endcap (EMEC), the LAr hadronic endcap (HEC), and the LAr forward calorimeter (FCal) [7]. The central LAr barrel also has a presampler layer, which estimates the energy lost before the particles reach the ECal.

All the detectors are non-compensating, sampling designs. Sampling detectors are designed in alternating layers of passive absorber and active readout. The passive layers are composed of some dense material (steel, lead, etc.) which, because of the high density of atoms, causes many interactions with the incoming particles, creating cascades of daughter particles. The active layers measure the energy of the showers—via mechanisms such as scintillation or ionization—and the process repeats several times, gradually reducing the energy of the shower with each layer and thereby stopping the particles. The non-compensating nature of the calorimeter means that energy is lost in each of these passive layers: the full energy read out by the active layers will not be that of

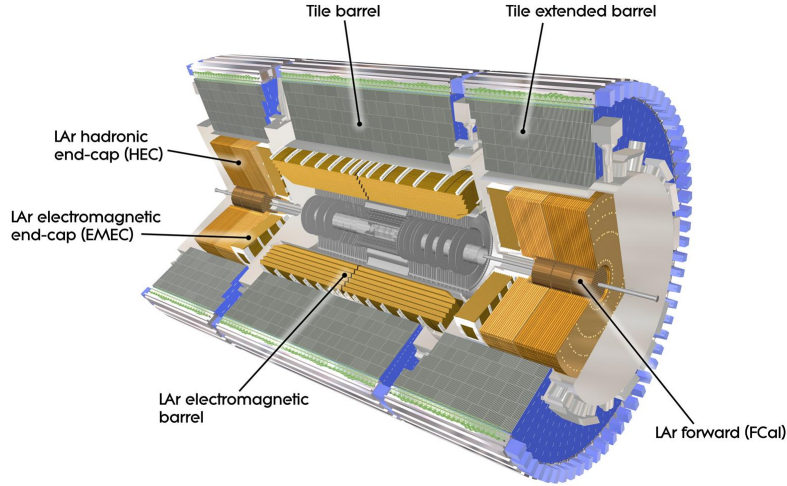


Figure 6.16: A computer generated image of the ATLAS calorimeter system, showing the locations of each different subdetector. Copyright CERN.

the incoming particles. Calibrations, described in later sections [*Ed: Fix that!*] can correct for the central value of this unmeasured energy, but fluctuations in the shower development inevitably mean that there is a price in terms of energy resolution [27]. The details of homogenous vs. sampling, and compensating vs. non-compensating designs depend greatly on the conditions of the collider, and the designs selected by ATLAS were chosen based on the compromises between expected performance gains and cost.

6.4.1 Electromagnetic Calorimeter

Like many of the other detectors, the ECal is composed of two main sections; the barrel and the endcaps [7]. The barrel covers the range $|\eta| < 1.475$, and occupy the space between 2.8 m and 4 m from the beamline. The detector is a total of 6.4 m long. Both use lead as the passive layer and liquid argon as the active material. A presampler covers the entire η range of the barrel.

The endcaps consist of two wheels, on either side of the detector, and cover the range $1.375 < |\eta| < 3.2$ and occupy the region between 330 mm and 2098 mm from the beamline³. A presampler also covers the region in front of the endcap.

The LAr calorimeters all operate via the measurement of ionization [19, 27]. As particles—particularly photons and electrons which interact predominantly electromagnetically—interact with the liquid argon, they knock free electrons and create ions. The high voltage applied across opposite ends of the detector drifts the free electrons to one side, where they can be measured. The passive

³Note that this is the first detector component listed that sits outside of the tracker volume in z , and so is not limited by the tracker's radial size.

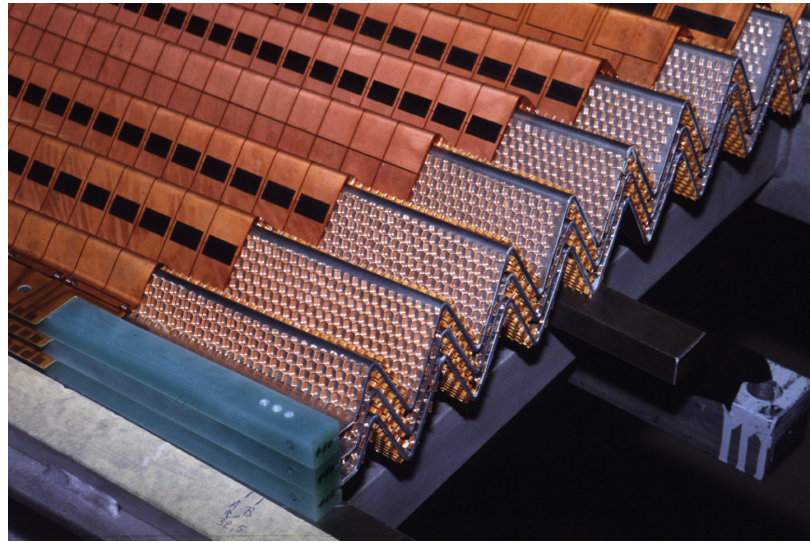


Figure 6.17: A photograph of the accordion structure used in the LAr barrel. Copyright CERN.

lead layers promote electromagnetic showering which can be read out by the active material, while also providing a large number of radiation lengths to absorb the energy of these particles.

The barrel system is composed of 2048 so-called “accordion-shaped” absorbers, instrumented with interleaved readout electrodes [7]. The characteristic accordion shape, displayed in Figure 6.4.1, is designed to reduce the drift time after a particle interacts but before the ionization energy has been collected. Depending on the η , there are between 3 and 4 separately read-out layers, in addition to the presampler, in each module. The size of the detector cells which are read out depends on the layer, as shown in Figure 6.4.1.

The endcap follows a similar design, separated into two sub-wheels per wheel [7]. The outer wheel (at lower values of $|\eta|$) is composed of 768 absorbers with three layers, and the inner wheel (at higher values of $|\eta|$) is composed of 256 absorbers with only two layers. The granularity of the outer wheel is similar to that of the barrel calorimeter, but the inner wheel has a coarser granularity.⁴ Figure 6.4.1 shows a photograph of one of the LAr endcaps after its installation in the detector.

Both detectors operate at voltages of approximately 2 kV [7]. The barrel occupies a cryostat shared with the solenoid, and is cooled by a nitrogen refrigerator system which operates at 80 K. The endcaps each share a cryostat with the HEC and FCal, and are cooled by a similar nitrogen system.

A benefit of using liquid argon as a readout material is that it is readily purified and relatively inexpensive, and so can easily be used in large volumes. A drawback is the long collection time of the ionization energy, typically of order 450 ns, which is complicated by the LHC’s design of collisions

⁴Note though that while the granularity is worse in η , the coordinate is asymptotic as θ increase and the physical granularity of the inner wheel is not worse.

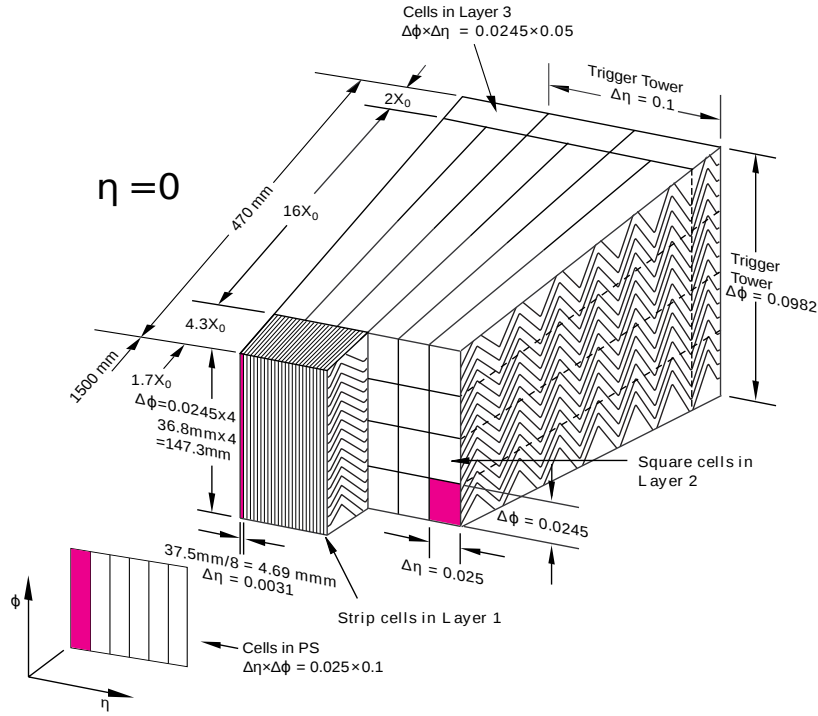


Figure 6.18: A drawing of a LAr module near $\eta = 0$. The relative size of each layer in the module, in both length and radiation lengths, is shown.

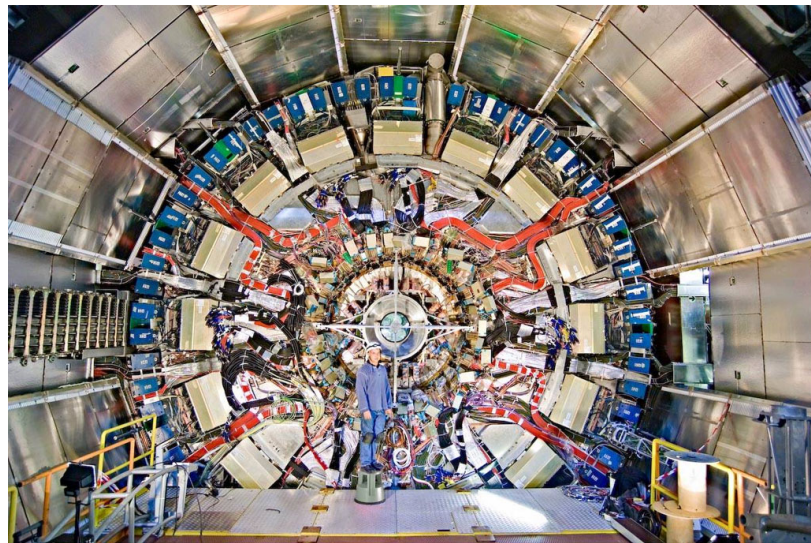


Figure 6.19: A photograph of the LAr endcap after installation in the cryostat system. Copyright CERN.

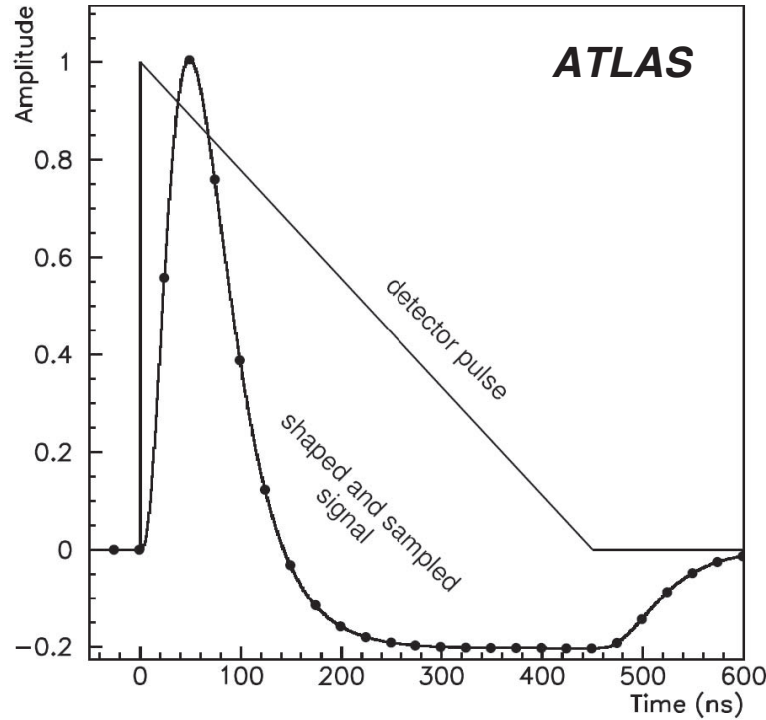


Figure 6.20: A plot of the LAr ionization pulse and the shaped output from the frontend electronics, including the negative energy region.

every 25 ns [7, 28]. This means that after a particle has left an energy deposit in the calorimeter in one bunch crossing, it remains for up to 16 subsequent bunch crossings. This effect is referred to as ‘out-of-time’ pileup. One solution to this issue is to exploit the very consistent and well understood characteristics of the ionization pulse, and to shape it (via the readout electronics) to compensate for out-of-time pileup. This is demonstrated in Figure 6.4.1: a bipolar $CR - (RC)^2$ analogue filter generates a fast time constant for the rise and fall (13 ns), resulting in a negative energy portion of the pulse [28]. This negative energy portion has the same integrated area as the positive portion: on average, the negative portion should cancel the in-time component of pileup from subsequent collisions [29]. The very predictable pulse shape also simplifies the readout: only the first five points need to be read out to predict the full shape, as shown in Figure 6.4.1.

As the liquid argon in the detector can be continuously filtered, there is no danger of damage due to radiation (in contrast to the CMS homogenous crystal calorimeter, which ‘darkens’ over time). Future upgrades include the goal of reading out at a higher rate and with potentially greater granularity, especially at the trigger level.

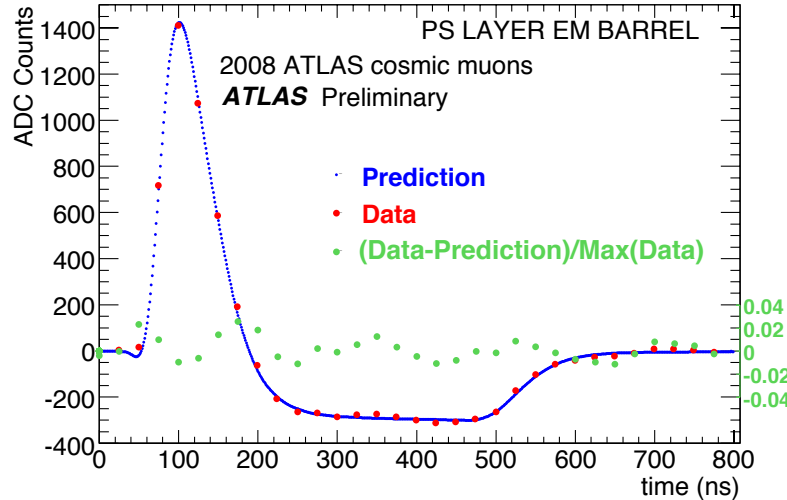


Figure 6.21: A plot the measured and predicted LAr energy distributions during a 2008 cosmic ray run.

6.4.2 Hadronic Calorimeter

The Hadronic Calorimeter is composed of four subsystems: the tile barrel, the tile extended barrel, the LAr hadronic endcap, and the LAr forward calorimeter.

The tile systems extend to $|\eta| < 1.7$ and sit behind the LAr electromagnetic calorimeter [7, 30]. The barrel detector is 5.8 m long, and each of the extended barrels are 2.6m long. The detectors each have an inner radius of 2.28 m and an outer radius of 4.25 m. The combined detector is shown, after installation the ATLAS cavern, in Figure 6.4.2. The detectors are composed of 64 wedge-shaped modules with size $\Delta\phi \approx 0.1$, an example of which is pictured in Figure 6.4.2. The detector is composed of alternating layers of steel plates and plastic scintillating tiles: by volume the steel-to-tile ratio is approximately 4.7:1 and is almost exactly periodic. The detector operates via similar principles to that of the ECal: particles (which at this depth in the detector are mostly hadrons) interact with the steel and produce showers of lower energy particles. These particles proceed through the scintillator: as they pass through a material where the speed of light is lower than their current speed, they emit scintillation light, which can be collected by readout fibers and read out by photomultiplier tubes. An example of one of the scintillating tiles is pictured in Figure 6.4.2. Like the ECal, the tile calorimeter contains three independently readout layers, which provies information about the longitudinal development of the particle shower. The front two layers are readout in $\Delta\eta \times \Delta\phi$ cells of approximately 0.1×0.1 for the front two layers, and and 0.2×0.1 for the third layer.

The hadronic endcap system is similar to the ECal, but is composed of alternating layers of

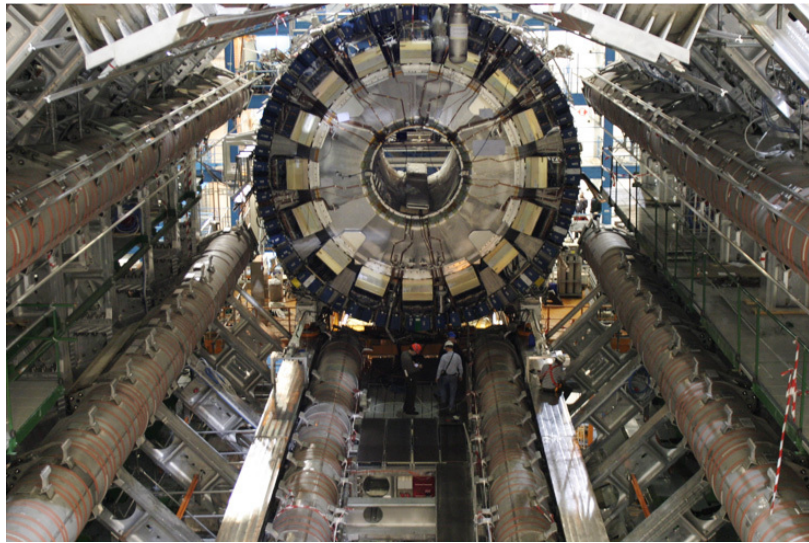


Figure 6.22: A photograph of the installation of the barrel tile calorimeter. Copyright CERN.

copper and liquid-argon with a flat design (in contrast to the ECal’s accordion shape) [7]. The detectors occupy the range $1.5 < |\eta| < 3.2$, and they share the end-cap cryostats with the EMEC and FCal. Each HEC endcap is composed of two wheels, each of which has two longitudinal layers. Each of the four wheels is cylindrical, with an outer radius of 2.03 m, and each of the wheels is composed of 32 wedge-shaped modules. The read-out cells have size $\Delta\eta \times \Delta\phi = 0.1 \times 0.1$ for $|\eta| < 2.5$, and 0.2×0.2 for larger values. The LAr ionization readout uses high-voltage set to 1800 V.

The ATLAS forward calorimeters are the final devices in the end-cap cryostats, and sit in the highest pseudorapidity, covering $3.1 < |\eta| < 4.9$ [7]. The FCal is composed of three 45 cm modules: FCal1 is an electromagnetic module, and FCal2 and FCal3 are hadronic modules. Copper is used as the absorber in FCal1, and tungsten is used in FCal2/3. All three use liquid argon as the active medium.

The HCal systems are all expected to perform very well in future LHC runs, even with increased pileup conditions. Upgrades to some of the readout systems to enable more rapid and more regular collection of data are the main goals in preparation for higher luminosity operations.

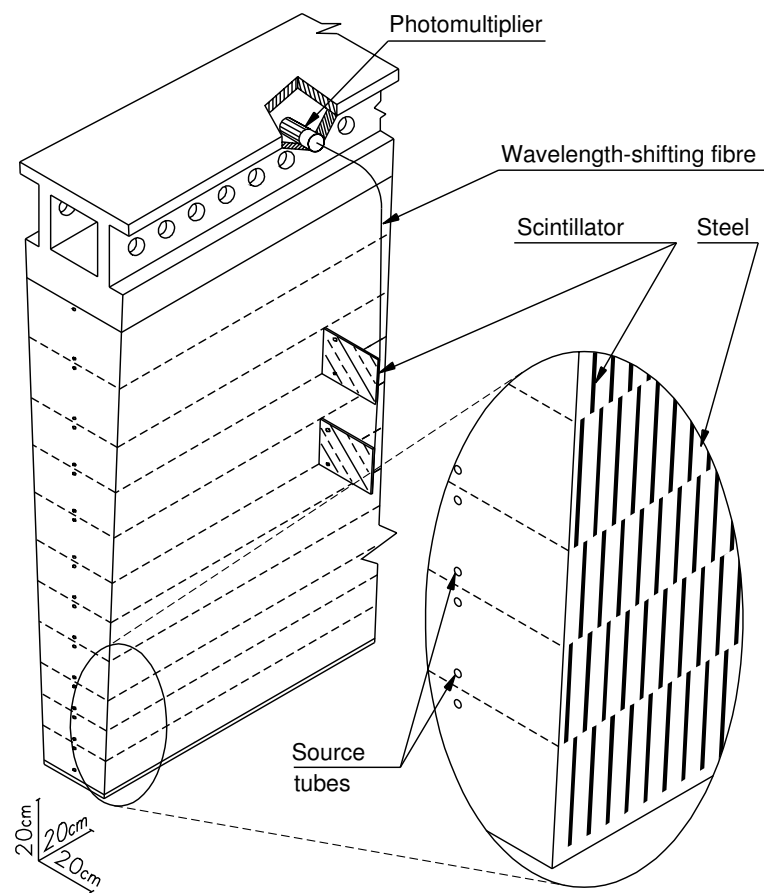


Figure 6.23: A drawing of one wedge of the tile detector.

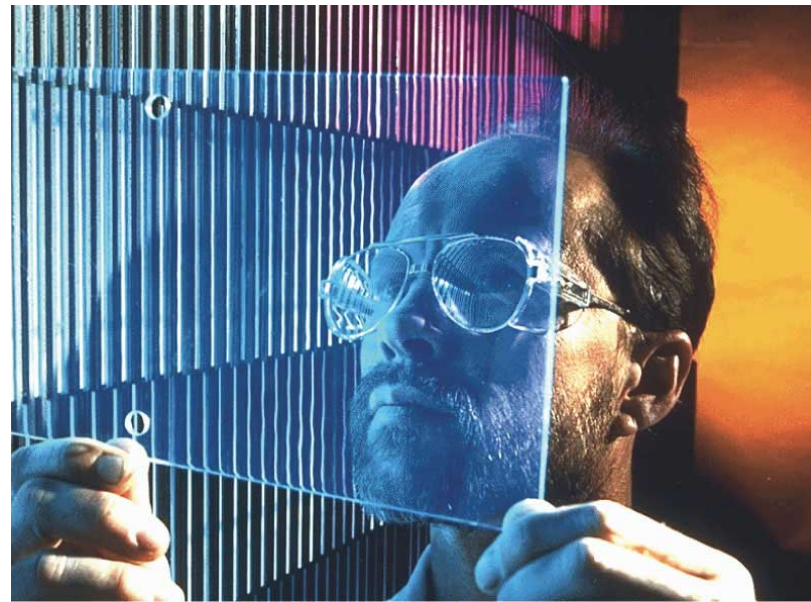


Figure 6.24: A photograph of one of the scintillating tiles which give the tile calorimeter its name. Copyright CERN.

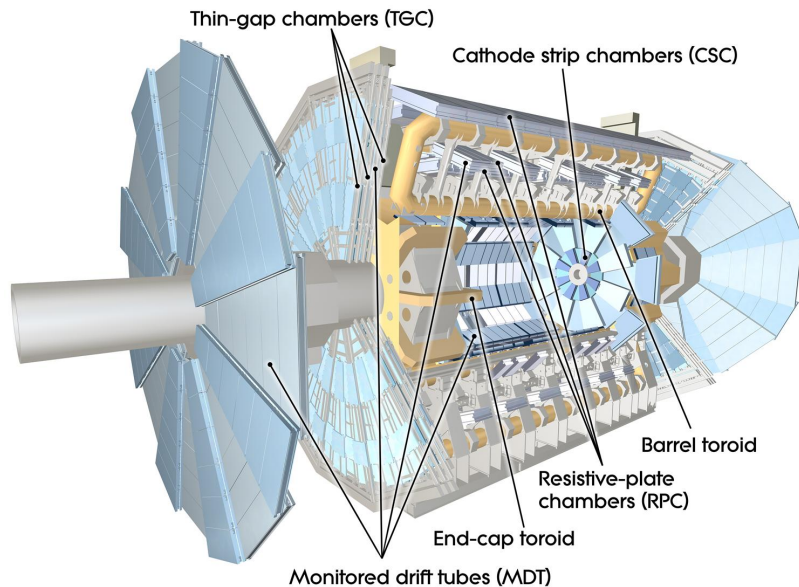


Figure 6.25: A computer generated image showing the locations of each of the muon spectrometer subsystems. Copyright CERN.

6.5 Muon Spectrometer

6.6 Triggering

6.7 Data Quality

Chapter 7

Jet Reconstruction with ATLAS

7.1 Clusters, Towers, and Tracks, Oh My

7.1.1 Cluster Calibration

7.2 Jet Calibration

7.3 Quark/Gluon Discrimination

7.3.1 Lots of subsections

...

Chapter 8

Seeing Color at the LHC

8.1 Motivation

8.2 Reconstructing Color

8.2.1 Finding Top Quarks

8.2.2 Origin Corrections

8.2.3 Resolution Effects

8.2.4 Track and Cluster Uncertainties

8.3 Measuring Color

8.3.1 Unfolding

8.3.2 Results

8.3.3 Future Prospects

...

Chapter 9

Searching for Supersymmetry with Super Jets

9.1 Motivation

9.2 Why Jet Substructure?

9.2.1 Total Jet Mass, and Other Variables

9.2.2 Jet Mass Templates

9.3 Constructing a Search

9.3.1 Background Estimates

9.3.2 Limits

9.3.3 Future Prospects

...

Chapter 10

Conclusions

...

Appendix A

A Long Proof

...

Bibliography

- [1] CERN, *Large Hadron Collider in the LEP Tunnel*, vol. 1. March, 1984.
<https://cds.cern.ch/record/154938?ln=en>.
- [2] ATLAS Collaboration, *ATLAS: letter of intent for a general-purpose pp experiment at the large hadron collider at CERN*. Letter of Intent. CERN, Geneva, 1992.
<https://cds.cern.ch/record/291061>.
- [3] *Proposal for a Dedicated Collider at the Fermi National Accelerator Laboratory*, tech. rep., Fermilab, 1983. <http://lss.fnal.gov/archive/misc/fermilab-misc-1983-02-02.pdf>.
- [4] *Perestroika and Particle Physics*, Science News (1988) .
<http://www.thefreelibrary.com/Perestroika+and+particle+physics.-a06519299>.
- [5] LHC Study Group Collaboration, T. S. Pettersson and P. Lefèvre, *The Large Hadron Collider Conceptual Design*, Tech. Rep. CERN-AC-95-05-LHC, CERN, Oct, 1995.
<https://cds.cern.ch/record/291782>.
- [6] M. Bajko et al., *Report of the Task Force on the Incident of 19th September 2008 at the LHC*, Tech. Rep. CERN-LHC-PROJECT-Report-1168, CERN, Geneva, Mar, 2009.
<https://cds.cern.ch/record/1168025>.
- [7] ATLAS Collaboration, *The ATLAS Experiment at the CERN Large Hadron Collider*, JINST **3** (2008) S08003.
- [8] CMS Collaboration, *The CMS experiment at the CERN LHC*, JINST **3** (2008) S08004.
- [9] European Committee for Future Accelerators and European Organization for Nuclear Research, *Towards the LHC Experimental Programme: 5-8 March 1992, Evian-les-Bains, France : LHC : Proceedings of the General Meeting on LHC Physics & Detectors*. CERN, 1992. <https://cds.cern.ch/record/236265/>.
- [10] *Early days: The Evian experiment meeting (archive)*, CERN Courier (2008) .
<http://cerncourier.com/cws/article/cern/35867>.

- [11] ATLAS Collaboration, W. Armstrong et al., *ATLAS: Technical proposal for a general-purpose $p\ p$ experiment at the Large Hadron Collider at CERN*, .
<http://atlasinfo.cern.ch/ATLAS/TP/tp.html>.
- [12] ATLAS Collaboration, *Archives of ATLAS Collaboration Records*, Tech. Rep. CERN-ARCH-ATLAS, CERN. http://library.web.cern.ch/archives/CERN_archive/guide/experimental_physics/LHC/isaatlas.
- [13] ATLAS Collaboration, *ATLAS detector and physics performance: Technical Design Report, 1*, Technical Design Report (1999) no. ATLAS-TDR-14, CERN-LHCC-99-014, 964 p.
<https://cds.cern.ch/record/391176>.
- [14] ATLAS Collaboration, *ATLAS detector and physics performance: Technical Design Report, 2*, Technical Design Report (1999) no. ATLAS-TDR-15, CERN-LHCC-99-015, .
<https://cds.cern.ch/record/391177>.
- [15] ATLAS Collaboration, *Expected Performance of the ATLAS Experiment - Detector, Trigger and Physics*, [arXiv:0901.0512 \[hep-ex\]](https://arxiv.org/abs/0901.0512).
- [16] ATLAS Collaboration, *Performance of the ATLAS Inner Detector Track and Vertex Reconstruction in the High Pile-Up LHC Environment*, Tech. Rep. ATLAS-CONF-2012-042, CERN, Geneva, Mar, 2012. <https://cds.cern.ch/record/1435196>.
- [17] R. Seuster, *Performance of the ATLAS Reconstruction Software with high level of Pileup in 2011*, *Journal of Physics: Conference Series* **396** (2012) no. 2, 022043.
- [18] G. Aad et al., *ATLAS pixel detector electronics and sensors*, *Journal of Instrumentation* **3** (2008) no. 07, P07007.
- [19] G. F. Knoll, *Radiation detection and measurement*. Wiley, New York, 3rd ed., 2000.
- [20] M. Capeans, G. Darbo, K. Einsweiller, M. Elsing, T. Flick, M. Garcia-Sciveres, C. Gemme, H. Pernegger, O. Rohne, and R. Vuillermet, *ATLAS Insertable B-Layer Technical Design Report*, Tech. Rep. CERN-LHCC-2010-013. ATLAS-TDR-19, CERN, Geneva, Sep, 2010.
<https://cds.cern.ch/record/1291633>.
- [21] ATLAS Collaboration, *Operation and performance of the ATLAS semiconductor tracker*, *Journal of Instrumentation* **9** (2014) no. 08, P08009.
- [22] F. Campabadal et al., *Design and performance of the ABCD3TA ASIC for readout of silicon strip detectors in the ATLAS semiconductor tracker*, *Nuclear Instruments and Methods in Physics Research Section A* **552** (2005) no. 3, 292 – 328.

- [23] ATLAS TRT Collaboration, *The ATLAS TRT electronics*, *Journal of Instrumentation* **3** (2008) no. 06, P06007.
- [24] ATLAS TRT Collaboration, *The ATLAS TRT Barrel Detector*, *Journal of Instrumentation* **3** (2008) no. 02, P02014.
- [25] ATLAS Collaboration, *Particle Identification Performance of the ATLAS Transition Radiation Tracker*, Tech. Rep. ATLAS-CONF-2011-128, CERN, Geneva, Sep, 2011.
<https://cds.cern.ch/record/1383793>.
- [26] ATLAS Collaboration, *TRT occupancy and tracking performance with large pileup*, Tech. Rep. ATL-COM-PHYS-2012-468, CERN, Geneva, May, 2012. <https://atlas.web.cern.ch/Atlas/GROUPS/PHYSICS/IDTRACKING/PublicPlots/ATL-COM-PHYS-2012-468/>.
- [27] R. Wigmans, *Calorimetry: Energy Measurement in Particle Physics*. Oxford University Press, 2000.
- [28] H. Abreu et al., *Performance of the electronic readout of the ATLAS liquid argon calorimeters*, *Journal of Instrumentation* **5** (2010) no. 09, P09003.
- [29] P. Loch, *Experimental Considerations for Jet Substructure Reconstruction– Present and Future*, tech. rep., University of Arizona, 2013.
<http://pages.uoregon.edu/soper/TeraJets2013/TeraJets2013Talks/loch.pdf>.
- [30] ATLAS Collaboration, *Readiness of the ATLAS Tile Calorimeter for LHC collisions*, *The European Physical Journal C* **70** (2010) no. 4, 1193–1236.
<http://dx.doi.org/10.1140/epjc/s10052-010-1508-y>.